ORIGINAL ARTICLE

Semi-solid plasticity and deformation control of superalloy investment casting

Zhengyi Ding[1] · Donghong Wang[1] · Bang Guan[1] · Jiayu Cui[1] · Da Shu[1] · Baode Sun[1]

Abstract

The deformation in superalloy investment casting under thermal-mechanical coupled stress results in significant waste of materials and energy. In order to accurately predict the deformation of castings, it is crucial to develop and apply mechanical models of both alloy and shell. The elastoplastic behavior of superalloy in a semi-solid zone is critical to the deformation during solidification. This study focuses specifically on the deformation of ring-to-ring castings with Ni-based superalloy K4169. To obtain the thermal-mechanical behavior of K4169 from solid region to semi-solid zone, physical simulated uniaxial compression is performed. The measured yield stress and plastic modulus are imported into the database for numerical simulation. Different thermal-mechanical models of both alloy and shell are compared. With elastoplastic model for alloy, considering the deformability of shell with elastic model, the maximum error is limited to 0.34 mm. Among groups of processing parameters, the deformation reaches the minimum when the initial temperature of alloy and shell are 1500 °C and 900 °C. The research on the semi-solid performance of the alloy and the development of thermal-mechanical models can provide theoretical insights for predicting deformation. Moreover, the research methodology holds promise for dimensional control of castings and can be transported to dimensional control problems upon solidification process with different kinds of materials and castings.

Keywords Investment · Casting · Semi-solid · Elastoplastic · Deformation · Prediction

1 Introduction

Investment casting has evolved significantly over thousands of years and is now a crucial technique in the manufacturing industry. In aircraft fabrication, especially parts in aero engines and gas turbines, investment casting has been widely utilized, due to its high dimensional accuracy, well surface finish, and the feasibility of castings with complex geometric properties [1, 2]. However, one of the major challenges in investment casting is the deformation caused by thermal-mechanical coupled stress, which can significantly impact the quality of castings, leading to massive waste of materials and lengthening of research and development periods. The control of deformation is traditionally performed with the iteration of trial-and-error process, which is time-consuming [3]. To address this challenge, accurate prediction of deformation is essential to reduce waste caused by experimental iteration of trial-and-error. Numerical approaches, such as finite element method, have been introduced into the prediction of deformation with the development of computational technology, which leads to a paradigm shift in casting design, from physical, experimental, and empirical to digital and virtual [4].

The majority of deformation in investment casting occurs during the period of solidification [5]. This deformation is primarily caused by the shrinkage of alloy, resulting from

✉ Donghong Wang
wangdh2009@sjtu.edu.cn

Zhengyi Ding
ki2317@sjtu.edu.cn

Bang Guan
guanbang@sjtu.edu.cn

Jiayu Cui
cui_jiayu@sjtu.edu.cn

Da Shu
dshu@sjtu.edu.cn

Baode Sun
bdsun@sjtu.edu.cn

1   Shanghai Key Lab of Advanced High-Temperature Materials
    and Precision Forming, School of Materials Science
    and Engineering, Shanghai Jiao Tong University, Shanghai
    200240, China

phase transformation and cooling contraction. The mechanical model of the alloy during the solidification process is essential to predict the deformation. Semi-solid zone, also known as "mushy zone," which lies between the nil-strength temperature and the solidus, is the most complicated region of deformation. Lewandowski and Overfelt [6] characterized the mechanical behavior of IN718 superalloy in a semi-solid state with mechanical test and microscopic observation and preposed the mechanism of grain boundary sliding caused by intergranular liquid films. Guo et al. [7] focused on the ductility of IN718 superalloy in the mushy zone, revealing the effect of segregation and grain size on welding performance. Lu et al. [8] established a quantified mechanical model of Al-4Cu-Mg alloy with compression experiment within the semi-solid zone, which revealed the mechanism of deformation behavior affected by microstructure. Afazov et al. [9] applied semi-solid performance in finite element method (FEM) simulation to investigate the relationship between residual stress and processing parameters.

Different models of the thermo-mechanical properties have been applied to the alloy in investment casting, including the pure elastic model, elastoplastic model [10], viscoelastic model [11], and elasto-viscoplastic model [12]. Wang et al. [4] simulated the deformation in elastoplastic model with experimental data and restricted the deformation of a complex model within CT6 grade specification. Panwisawas et al. [12] modeled the stress and strain evolution during the solidification process of CMSX-4 alloy with elasto-viscoplastic model, which revealed the occurrence of plasticity in two distinct regimes with different mechanisms during this process. Galles et al. [13] applied the finite element inverse method on elastoplastic model, resulting in a deformation compensating model with residual deformation of only 2% of the original model. Qiu et al. [14] focused on specific dimension on turbine blade margin plate by simulating with different processing parameters, reducing the shrinkage of margin plate by 21.8%.

The interaction between alloy and ceramic shell is also a crucial factor influencing the deformation. During the cooling process, as the alloy shrinks, the inner side of shell supports the alloy structurally, obstructing the shrinkage. The extent of this obstruction can be referred to as the deformability of the shell material. There are varieties of models that represent the mechanical behavior of shell materials in the casting process. Vacant model assumes zero modulus of the shell, so that the alloy contracts freely, which is practical in sand casting. Rigid model assumes zero deformation of the shell or infinitive stiffness, which is more accurate in

die casting. These models can reduce calculation in stress field simulation, but result in large accuracy loss in prediction deformation in investment casting [4]. Galles and Beckermann [15] investigated the impact of shell on pattern allowance in sand casting, identified the importance of dilation, and gave a quantified model. Yan et al. [16] took the deformation of shell into consideration with FDM simulation, resulting in agreement with practical cases in slot-board material. Pattnaik et al. [17] measured thermo-mechanical properties of the ceramic shell and applied these properties in numerical simulation using COMSOL Multiphysics. Neto et al. [18] researched the distortion of castings with shell materials with different deformability, proving the relevance in investment casting of alloys. Previous studies have demonstrated the correlation between casting deformation and the mechanical properties of the alloy, as well as the interaction between the alloy and the mold shell. However, a definitive conclusion regarding the most suitable deformation model for accurately predicting the deformation remains elusive.

In this paper, the deformation of ring-to-ring castings with Ni-based superalloy K4169 is researched. The thermo-mechanical properties of both alloy and shell are measured. Uniaxial compression based on physical simulation of casting process is carried on Ni-based superalloy K4169, while the heat expansion of fiber-reinforced mullite is measured. The deformation with both linear elastic and elastoplastic models on alloy, as well as rigid and elastic shells, are compared. The relationship between processing parameters, including alloy temperature and shell preheated temperature, and the dimensional distortion of casting, including shrinkage compensating coefficient and ovality, are researched with numerical simulation. Finally, a verification experiment is performed to inspect the accuracy of the prediction of deformation.

2 Materials and methods

2.1 Materials

In this research, the experimental alloy material is K4169 Ni-based superalloy. The composition is shown in Table 1.

This composition benefits from the strengthening phase γ' (Ni$_3$(Al, Ti)) and γ' (Ni$_3$Nb), which provides high tensile strength, hardness, and fatigue life [19]. With these great properties, this composition is widely applied in investment casting, especially in the aerospace field.

Table 1 The nominal composition of K4169 Ni-based superalloy

Elements	Al	C	Cr	Fe	Mo	Nb	Ti	Ni
Composition (wt%)	0.50	0.02	18.3	18.9	3.0	5.0	0.97	Bal.

Table 2 The composition of fiber-reinforced mullite shell

Components	Sintered mullite powder	Silica sol	Aluminum silicate fiber	Lignocellulose	Defoaming agent
Composition (wt%)	63	32.3	4	0.5	0.2

Mullite is a widely used material in ceramic shell for investment casting. High-temperature performance is critical in casting process, which can avoid cracking and control distortion [20]. Adding extra thickness could strengthen the shell, but it leads to difficulty in post-processing and pinholes at the surface [21]. By introducing fibers such as aluminum silicate [22] and betel nut fiber [23], the strength and damage tolerance of mullite can be significantly improved. The composition (wt%) of fiber-reinforced mullite shell in this research is shown in Table 2.

The SEM image of fiber-reinforced mullite is shown in Fig. 1a compared with non-reinforced one in Fig. 1b. Coefficient of thermal expansion (CTE) is measured with Linseis DIL L75 PT horizontal dilatometer, and the result is shown in Fig. 1c.

2.2 Mechanical models in casting numerical simulation

Castings with complex structures, such as ring-to-ring structure and multi-thickness section, generate heterogeneous temperature gradients, leading to uneven cooling, which results in internal stress. The ideal model of casting is to shrink homogeneously during the cooling process, so that a simple scaling factor can compensate the dimensional deviation from the shell to the finished casting. However, due to unbalanced internal stress, the prediction of deformation with simple factor is almost impossible. Additionally, in complex ring-to-ring structures, geometric constrain, interacting with the constrain of shell, makes the result away from free shrinkage. Superalloy investment castings usually have high-quality demand, with little dimensional tolerance, so misprediction can result in massive waste.

In order to predict deformation accurately, numerical simulation has been widely applied in investment casting. The thermo-mechanical behavior of alloys and shells is generalized and numerically modeled, so that the deformation can be simulated digitally. Versatile models of the strain–stress property have been established, including the pure elastic model, elastoplastic model, viscoelastic model, and viscoplastic model.

The pure elastic model shows a pure linear relationship between strain and stress, which is simple for computing. However, the yield stress near solidus line is very low; therefore, plastic deformation is not negligible in the solidification process. This model is only valid in the elastic region, hence inadequacy for predicting deformation in complex casting structure. In this model, the relationship between strain ε and stress σ can be easily described with Hooke's law with Young's modulus E:

$$\varepsilon = \sigma/E \tag{1}$$

Viscoelastic and viscoplastic models are related to creep behavior. Nonetheless, given the rapid cooling rate (ranging from about 0.2 to 1.3 °C/s) [24] without insulation, the cooling process is short without insulation, which results in negligible creep. Therefore, these models are excessively complex and time-consuming for numerical, which impedes their utilization in investment casting numerical simulation.

The elastoplastic model is a well-balanced model between complexity and accuracy in deformation prediction. At the
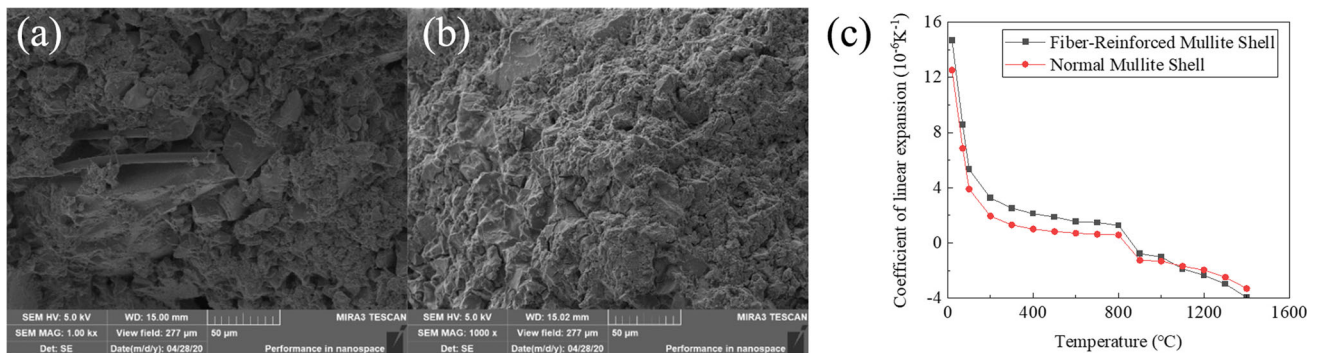

Fig. 1 **a** Microstructures of fiber-reinforced mullite, **b** normal mullite, and **c** CTE of mullite

beginning of stress load, the material shows linear elasticity, which can be recovered instantaneously after unloading. Once the load exceeds a specific criterion (which is well known as yield stress in 1-D model), the material undergoes plastic deformation, resulting in a permanent strain that persists even after the external load, or ceramic shell constrain for investment casting, is removed. The majority of plasticity can be described by the Holloman strain-hardening equation:

$$\sigma = K\varepsilon^n \tag{2}$$

In the equation, K is the hardening index, while n is the hardening exponential, which varies between 0 and 1 under different conditions. By considering the pure elasticity before yield ($\sigma \leq \sigma_y$), elastoplastic model can be described as follows:

$$\varepsilon = \begin{cases} \sigma/E & \sigma \leq \sigma_y \\ [(\sigma - \sigma_y)/K]^{1/n} + \sigma_y/E & \sigma > \sigma_y \end{cases} \tag{3}$$

In simulation softwares that support the elastoplastic model, the model is simplified into a bilinear model using a secant or tangent approximation of the exponential curve. By replacing the hardening index K with plastic modulus P, the simplified strain–stress model in actual numerical simulation can be demonstrated as follows:

$$\varepsilon = \begin{cases} \sigma/E & \sigma \leq \sigma_y \\ (\sigma - \sigma_y)/P + \sigma_y/E & \sigma > \sigma_y \end{cases} \tag{4}$$

2.3 Semi-solid properties measurement

A part of the thermo-mechanical and physical properties of K4169 alloy, such as liquidus, solidus, Young's modulus, and Poisson's ratio, can be calculated within casting simulation software ProCAST. However, other properties, including yield stress and plastic modulus, which is indispensable in simulations with elastoplastic model, are not available. Moreover, unlike Young's modulus, these properties are sensitive to microstructures [25], so thermodynamic calculation may lead to large errors.

The thermal-mechanical performance of this alloy is measured with uniaxial compression in the Gleeble 3800 thermal-mechanical physical simulation system. The measured temperature points range from 600 to 1200 °C, with intervals 100 °C below 1000 °C and 50 °C above, respectively. In order to obtain accurate performance for alloy solidification, a physical simulation approach is applied in this research. The compressive sample is heated 20 °C/s from room temperature to testing temperature, held for 5 min, and then compressed at 10^{-3}s^{-1} strain rate. The physical simulation setup is shown in Fig. 2a, while the required dimension of compressive sample is shown in Fig. 2c.

The nil-strength temperature (NST) is crucial in the performance of semi-solid zone [26], which is also measured in this experiment. The dimensional requirement of specimen is shown in Fig. 2b. A tiny load of 3MPa is applied on the specimen at room temperature. The specimen is heated to 1200 °C with a constant rate of 20 °C/s and then heated to the fracture point with a lower heating rate of 3 °C/s. The temperature at which specimen fractures is the NST of the specimen.

2.4 Numerical simulation setup

A featured ring-to-ring casting model, which is inspired from the ring set structures in aero engines, is used in this study. The dimension of this model is shown in Fig. 3. In this research, the elastoplastic model and linear elastic model for alloy are compared to study the effect of plasticity on the deformation of castings. Linear elastic shell is compared to rigid shell, in order to quantify the shell deformability and its impact on the dimension of casting.

The simulation is set in ProCAST. Thermal-mechanical properties of alloy and shell measured in the previous section are imported into the database. Other required properties of alloy, including heat capacity, heat conductivity, solid
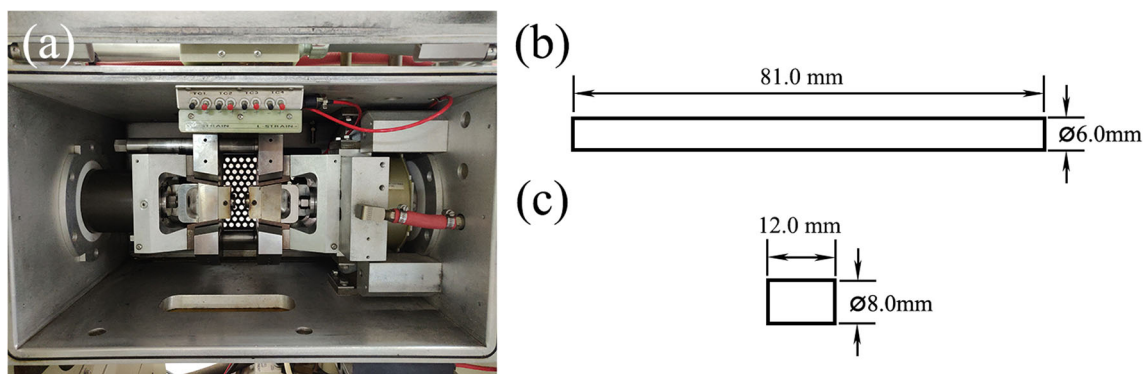
Fig. 2 Physical simulation setup. **a** Gleeble 3800 system. **b** The dimension of NST sample. **c** The dimension of compressive sample

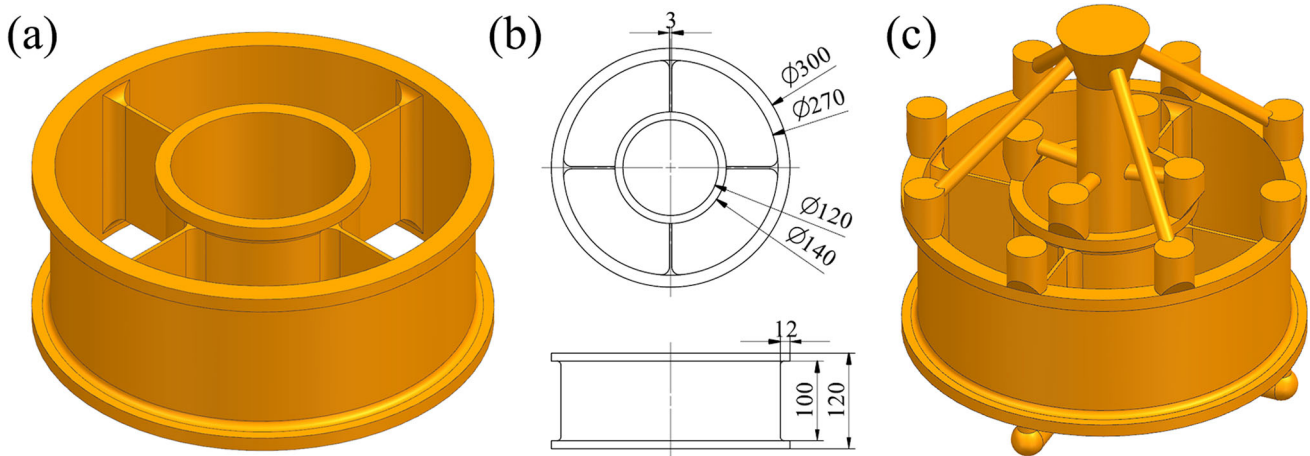81.0 mm
Ø6.0mm

12.0 mm
Ø8.0mm

Fig. 3 **a** Ring-to-ring casting model, **b** dimension of the model (unit: mm), and **c** model with gating system

fraction, and linear expansion coefficient, are calculated with the built-in thermodynamic calculation model. Shell properties are partially extracted from the database in ProCAST.

Other boundary conditions are listed below. Alloy temperature is 1500 °C, while shell temperature is 1000 °C. Inlet time is 5 s. Heat transfer coefficient at the casting-shell boundary is modified from IN738-mullite data in the ProCAST database.

3 Result and discussion

3.1 Thermomechanical performance of K4169

The result of physical simulated compression test is shown in Fig. 4ab. Nil-strength temperature results of two parallel groups are shown in Fig. 4c. The results are 1264 °C and 1262 °C, respectively, so NST is measured to be 1263 °C.

Young's modulus, yield stress, and plastic modulus are calculated from the result above, which are shown in Fig. 5. Young's modulus obtained from the thermodynamic

calculation in both ProCAST and JMatPro is compared with experimental result, along with the plastic modulus, which is typically assumed as 1/20 of Young's modulus by default. The result shows that measured Young's modulus closely matches the thermodynamic calculation result. Plastic modulus is similar to the tendency of the emulated "calculation results," but the value is significantly different. Yield stress is far from the calculation results, which might be attributed to the difference in microstructure between the as-cast state and heat-treated state.

Yield stress and plastic modulus are chosen to replace the result from thermodynamic calculation and imported into the database, for numerical simulation in the next sections. Semisolid regions between 1200 °C and NST are completed with calculated data.

3.2 Elastoplastic deformation of alloy

The comparison between elastoplastic and linear elastic models is shown in Fig. 6. The deformation in the elastoplastic model is significantly smaller than the linear elastic model.
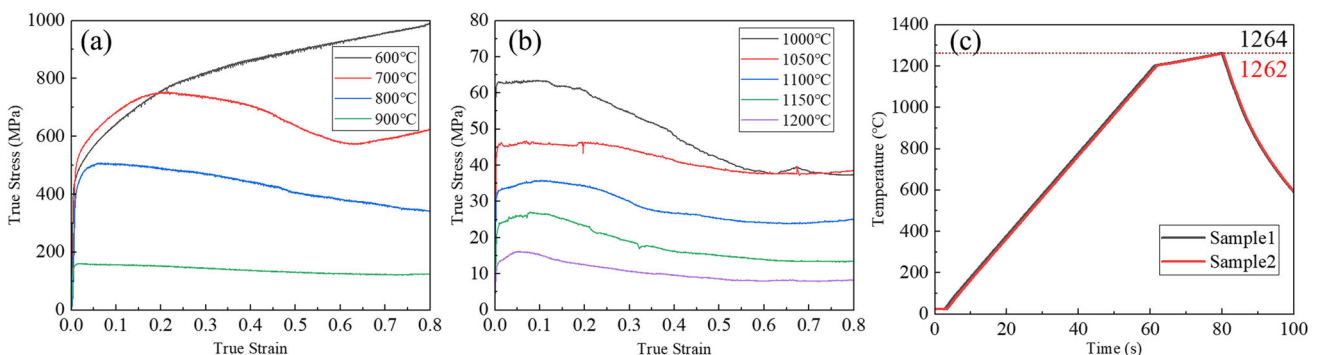

Fig. 4 Results of physical simulation tests. **a** Low-temperature thermal compression, **b** high-temperature and semisolid thermal compression, and **c** nil-strength temperature measurement
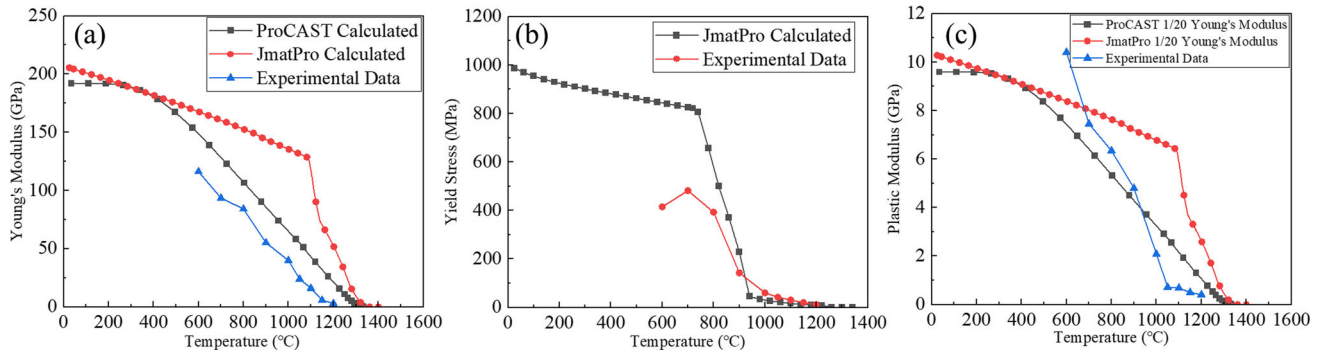
Fig. 5 Young's modulus, yield stress, and plastic modulus of K4169

Except for the gating system, both models show the largest deformation at the flange of outer ring under risers, which are 1.94 mm and 2.45 mm, respectively. It is also obvious that the deformation on both rings is not contracting evenly, due to the support of a thin plate between rings.

Five critical points of the ring-to-ring model are selected to quantify the variation of different dimensions in the model. Points 1 and 2 are set for the outer ring diameter and roundness, points 3 and 4 are set for the inner ring, and point 5 is for the thin plate between the two rings. The deformation evolution of 5 points are shown in Fig. 7.

The deformation of point 5 on the thin plate is the smallest in both models. The elastoplastic model shows that the deformation of the inner ring (points 3 and 4) is larger than the outer ring (points 1 and 2), while the linear elastic model gives controversial outcomes. In the elastoplastic model, the displacement is smoothly evolving with cooling process, while in the elastic model, there are discontinuous points in the

deformation of points on both rings. With the contraction of both casting and shell during the process of cooling, the interspace between casting and shell occurs. When plasticity is not considered, there is no permanent deformation, so the stress relaxes instantly when the stress occurs, causing more sudden jumps in displacement, which may lead to significant error.

3.3 The deformability of shell

The simulation result with both elastic and rigid models of shell is shown in Fig. 8. The deformation with elastic shell is significantly larger than rigid shell, with the maximum of 1.94 mm and 1.18 mm, respectively. The maximum deformation of shell is 1.45 mm, which is in direct contact with the point of maximum deformation on the casting. The deformation at same point is not the largest in rigid shell, which shows
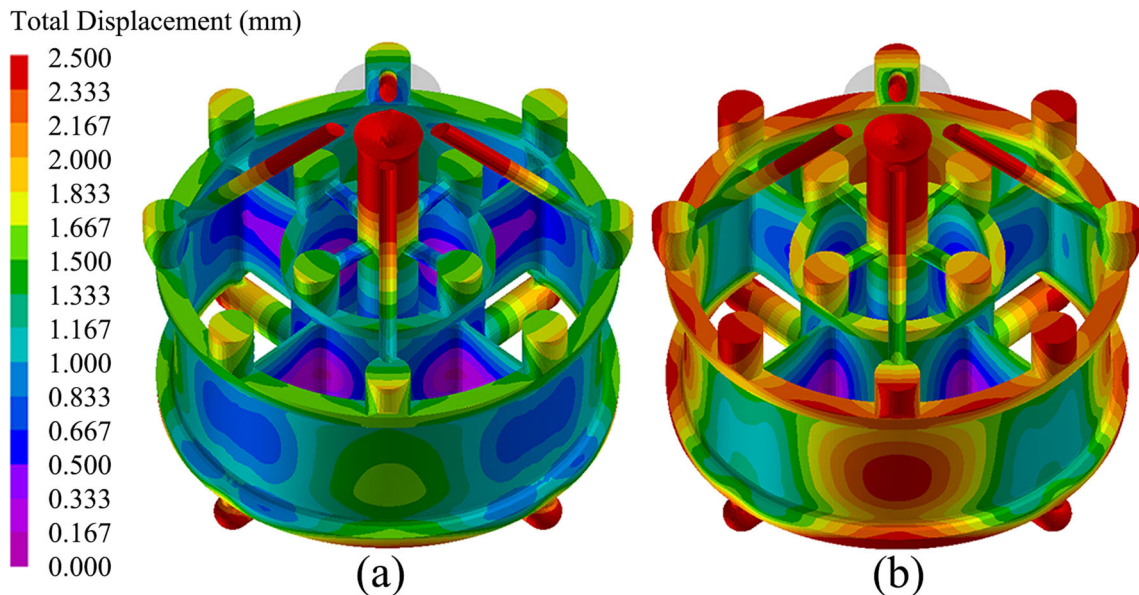

Fig. 6 Deformation result with different alloy models. **a** Elastoplastic model and **b** linear elastic model
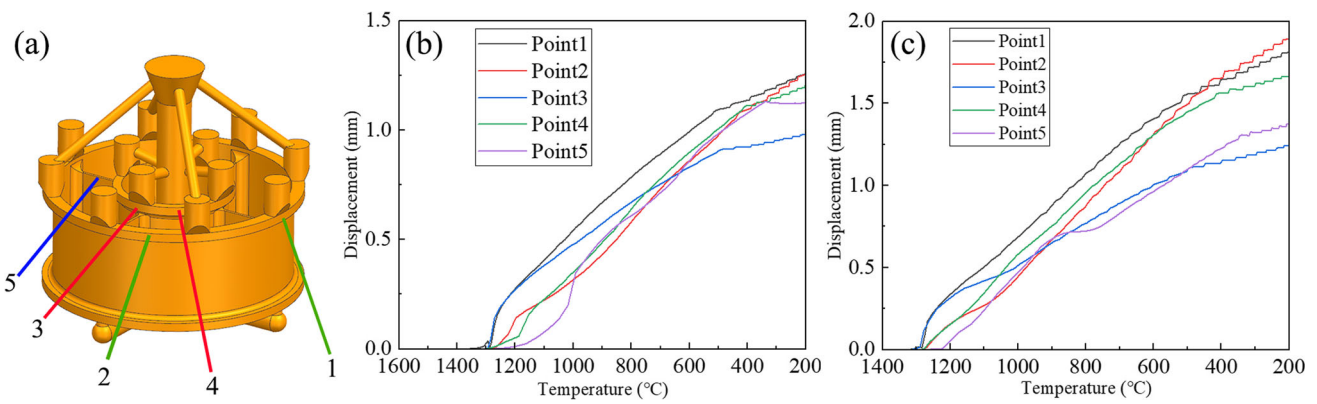
Fig. 7 Critical points result with different alloy models. **a** Positions of critical points in ring-to-ring model, **b** elastoplastic model, and **c** linear elastic model

the consequence of miscalculation without the deformability of shell.

The deformation in the x-axis is shown in Fig. 9a and b. The shrinkage with linear elastic shell is significantly larger, because the deformability of the shell is considered. In contrast, in the case with rigid shell, the constraint of shell is unlimited, which supports the casting from the inner side and impedes shrinkage. The deformation process of two points at the inner wall and outer wall is examined. Figure 9c shows the shrinkage of the inner wall during the cooling process in both models. The shrinkage is negative in both models as the shrinkage of thin plate stretches the inner wall outward. After reaching 1015 °C, the deformability of shell takes control and restricts the deformation after about 600 °C. Figure 9d shows the outer wall of the casting. With linear elastic shell, after reaching 1230 °C, as the alloy solidifies, the casting separates from the shell and shrinks inward, while the shell "shrinks" outward. The deformability of shell enhanced the stretch on the outer wall, leading to larger shrinkage after 1090 °C, compared to the rigid shell model.

3.4 The effect of processing parameters on deformation

The result of simulations with different alloy initial temperatures is presented in Fig. 10. For both the inner and the outer rings, the deformation of the casting reaches minimum when the initial temperature is set at 1500 °C, while the uniformity of deformation improves with increasing temperature. Figure 11 shows the maximum and the minimum deformation on the outer ring. It can be observed that the deformation is almost identical until the casting cools down to about 500 °C. After reaching this temperature, there is a sudden change in the deformation rate with both 1500 °C and 1550 °C initial temperatures, which can be attributed to the transition from plasticity to elasticity in certain areas near the outer ring.

The effect of shell preheated temperature is illustrated in Fig. 12. The deformation reaches the minimum at 900 °C, with the best homogeneity among these cases. The maximum and the minimum deformation on the outer ring are shown in Fig. 13. A sudden change in the deformation rate
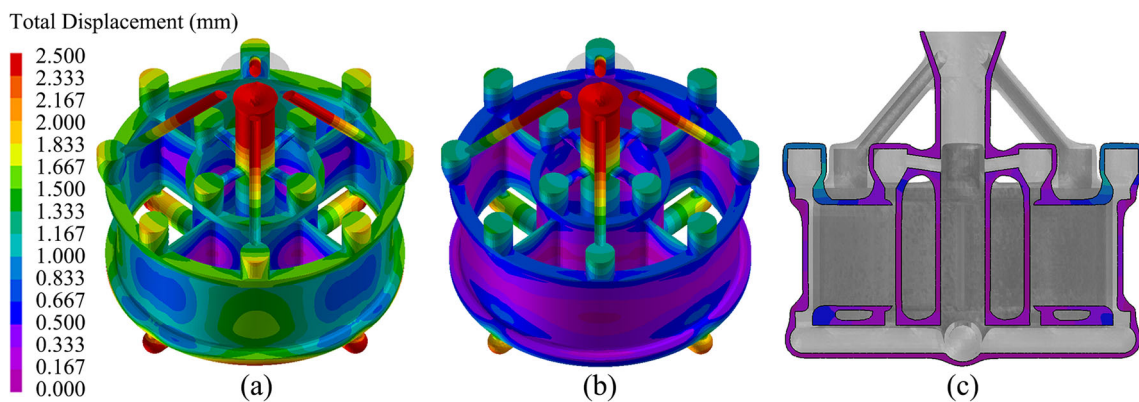

Fig. 8 Deformation with different shell models. **a** Linear elastic model, **b** rigid model, and **c** shell deformability in linear elastic
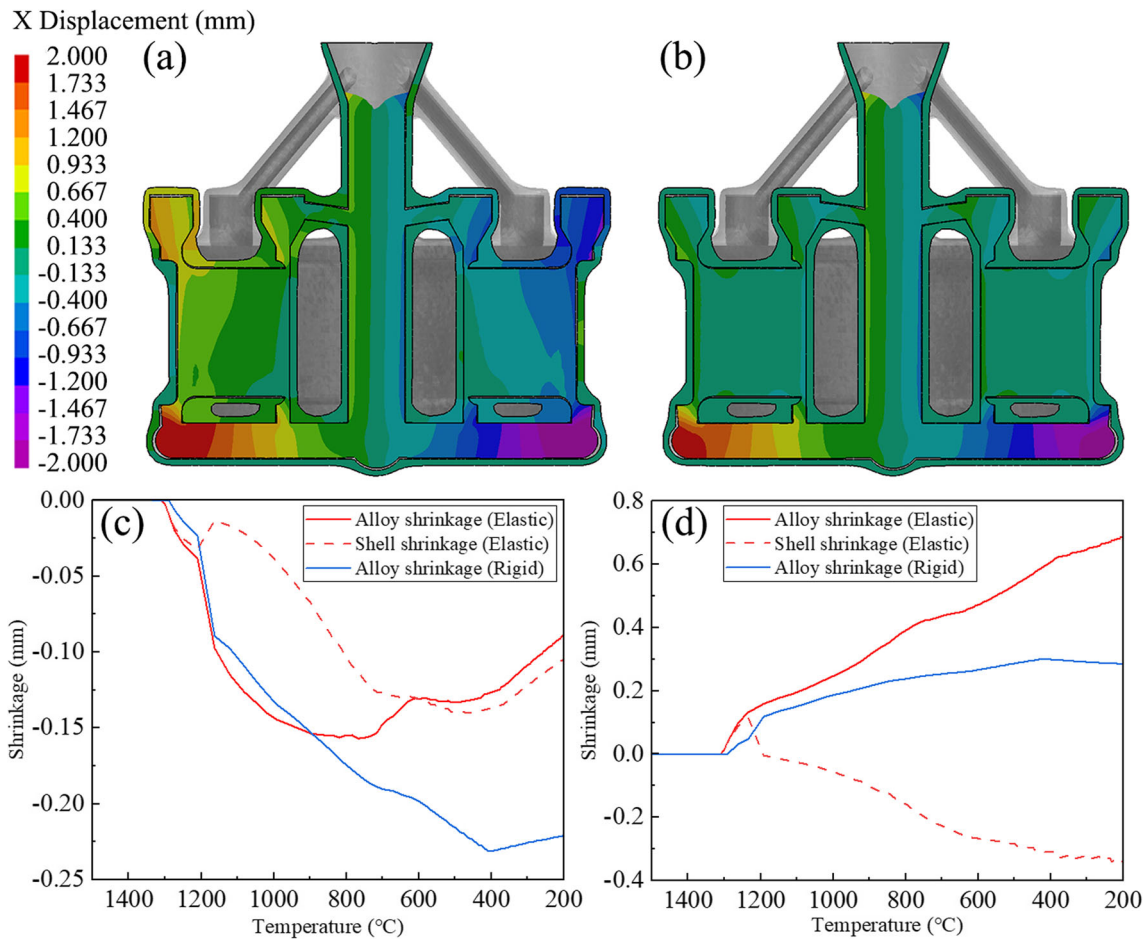
Fig. 9 *X*-axis section and shrinkage result. **a** Linear elastic model, **b** rigid model, **c** inner wall shrinkage, and **d** outer wall shrinkage

occurs in all cases at different temperatures. Specifically, in the 900 °C case, the transition occurs at around 500 °C, while in the 800 °C and 1000 °C cases, the transition happens at approximately 390 °C and 380 °C, respectively.

The quantified deformation result of both inner and outer rings is shown in Table 3. The diameter is the average amount of the whole ring, while roundness is the difference between the maximum and minimum radius of the ring. The initial temperature of both the alloy and shell has a significant impact on the dimension of final casting. With the alloy temperature at 1500 °C and shell temperature at 900 °C, the deformation reaches the minimum, while roundness can be improved slightly by raising the alloy temperature to 1550 °C.
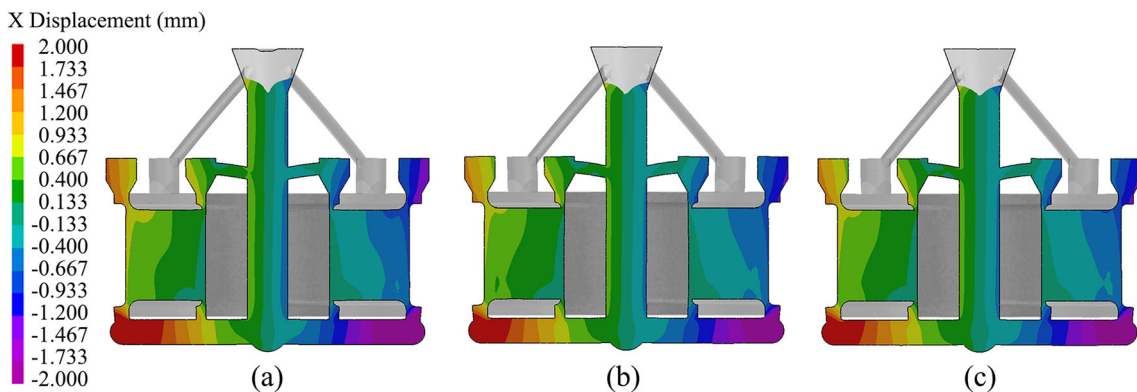
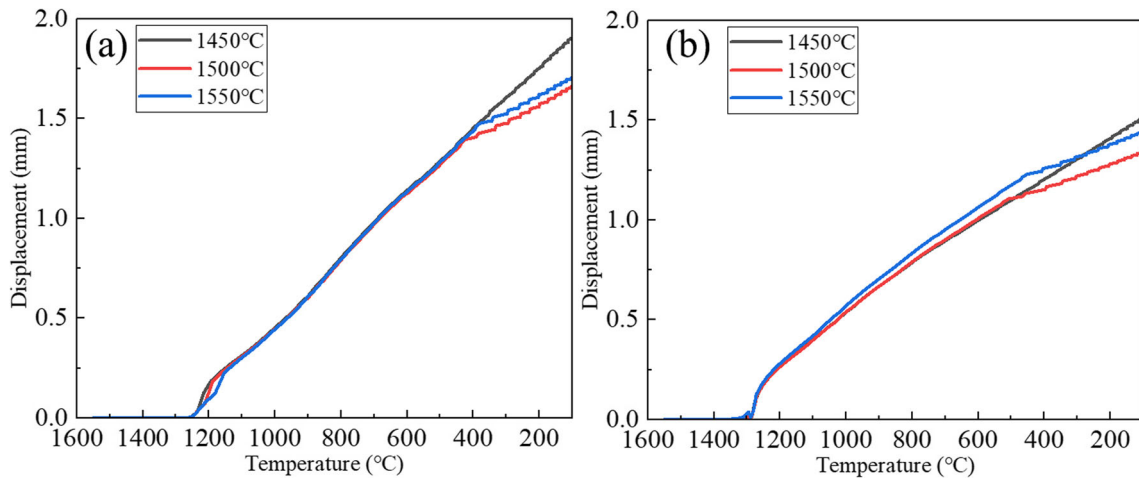**Fig. 10** Deformation with different alloy initial temperatures. **a** 1450 °C, **b** 1500 °C, and **c** 1550 °C

Fig. 11 Deformation on outer ring flange with different alloy initial temperatures. **a** Maximum and **b** minimum
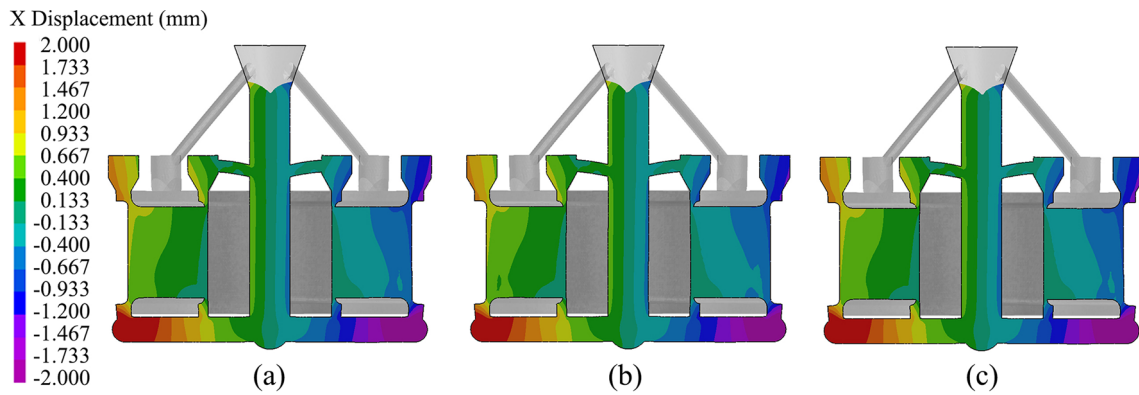

Fig. 12 Deformation with different shell preheated temperatures. **a** 800 °C, **b** 900 °C, **c** 1000 °C
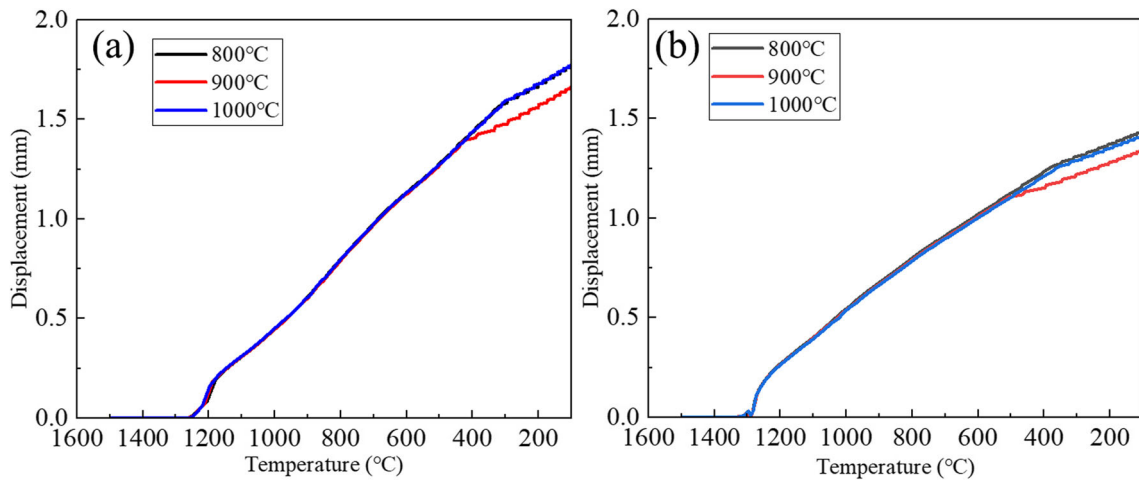

Fig. 13 Deformation on outer ring flange with different shell preheated temperatures. **a** Maximum and **b** minimum

Table 3 The deformation of rings with different processing parameters

No.	Alloy temperature (°C)	Alloy temperature (°C)	Outer ring diameter	Inner ring diameter	Outer ring roundness	Inner ring roundness
1	1500	900	297.50	138.46	0.33	0.28
2	1450	900	297.12	138.25	0.41	0.35
3	1550	900	297.38	138.40	0.29	0.24
4	1500	800	297.32	138.35	0.35	0.29
5	1500	1000	297.34	138.35	0.37	0.30

Unit: mm

3.5 Experimental verification

In order to verify the simulated result, the ring-to-ring casting model is manufactured in the real world at 1500 °C alloy temperature and 900 °C shell temperature, with no shrinkage compensation in casting process. The finished casting is 3D scanned, and a comparison is made with the simulation result with different strain–stress models of both casting and shell.

Taking the outer ring flange as a critical dimension, the comparison between the real casting and simulations with different models are shown in Fig. 14b. Among the various combinations of different strain–stress models, the elastoplastic-elastic models for alloy and shell exhibit the best predictive performance. The "periodic" trend in deformation, attributed to the symmetry of the casting, is well predicted by all these models. Prediction errors are primarily observed at positions corresponding to thin plates and risers, which are located at $90k°$ and $(90k + 45)°$ angles, respectively. The maximum error of 0.34 mm occurs at about 180°, specifically at the joints of the ring, thin plate, and riser. To achieve more accurate predictions, further refinement of constitutive models, along with additional research on the deformation in wax pattern fabrication and other processes, is crucial.

4 Conclusion

In this research, the elastoplastic model and linear elastic model are applied on alloy and shell for numerical simulation of deformation in investment casting. The following conclusion can be drawn:

- By applying elastoplastic and linear elastic models to alloy and shell respectively, in combination with thermal-mechanical properties measurements, the simulation closely aligns with the experimental results, with a maximum misprediction of 0.34 mm. This performance surpasses that of the elastic model for alloy and rigid model for shell.
- The initial temperatures of both alloy and shell significantly impact the deformation. The average deformation reaches minimum with alloy initial temperature at 1500 °C and shell preheated temperature at 900 °C.
- The measurement and modeling of mechanical properties for both the alloy and the shell contribute to enhancing the accuracy of numerical simulation. Consequently, these findings can be generalized for dimensional prediction and control upon solidification process for various materials and castings.
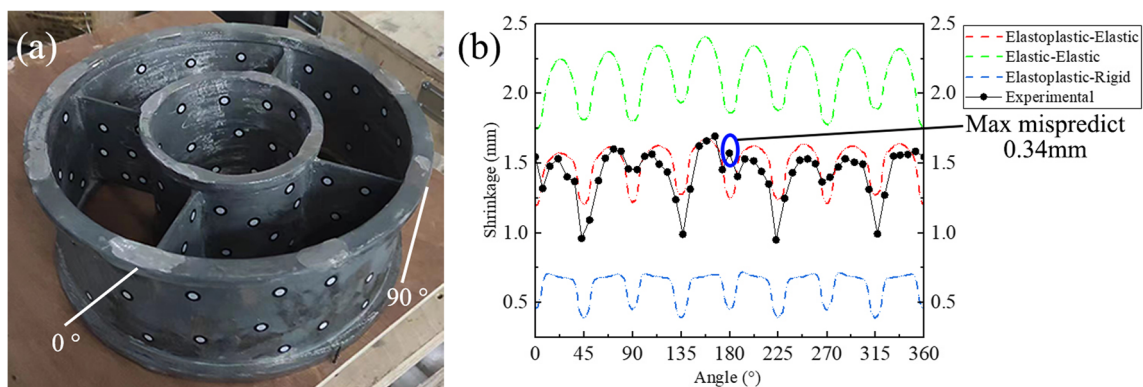
Fig. 14 Casting for verification. **a** Final product and **b** radial shrinkage at the flange of outer ring

Declarations

Competing interests The authors have no relevant financial or non-financial interests to disclose.

References

1. Tamta K, Karunakar DB (2021) Development of hybrid pattern material for investment casting process: an experimental investigation on improvement in pattern characteristics. Mater Manuf Process 36(6):744–751. https://doi.org/10.1080/10426914.2020.1854471

2. Gill SS, Kaplas M (2009) Comparative study of 3D printing technologies for rapid casting of aluminium alloy. Mater Manuf Process 24(12):1405–1411. https://doi.org/10.1080/10426910902997571

3. Galles D, Beckermann C (2017) Prediction of distortions and pattern allowances during sand casting of a steel bracket. Int J Cast Met Res 30(3):133–147. https://doi.org/10.1080/13640461.2016.1262984

4. Donghong W, Yu J, Yang C, Hao X, Zhang L, Peng Y (2022) Dimensional control of ring-to-ring casting with a data-driven approach during investment casting. Int J Adv Manuf Technol 119(1):691–704

5. Cannell N, Sabau AS (2005) Predicting pattern tooling and casting dimensions for investment casting, phase II. Report, Edison Materials Technology Center (EMTEC)

6. Lewandowski M, Overfelt R (1999) High temperature deformation behavior of solid and semi-solid alloy 718. Acta Mater 47(18):4695–4710

7. Guo H, Chaturvedi MC, Richards NL (1999) Effect of boron concentration and grain size on weld heat affected zone microfissuring in Inconel 718 base superalloys. Sci Technol Weld Join 4(4):257–264. https://doi.org/10.1179/136217199101537761

8. Lu Y, Li M, Huang W, Jiang H (2005) Deformation behavior and microstructural evolution during the semi-solid compression of Al-4Cu-Mg alloy. Mater Charact 54(4–5):423–430

9. Afazov S, Becker A, Hyde T (2011) Fe prediction of residual stresses of investment casting in a bottom core vane under equiaxed cooling. J Manuf Process 13(1):30–40

10. Bathe, K-J (2006) Finite element procedures. Klaus-Jurgen Bathe

11. Labergère C, Long M, Badreddine H, Niane N, Grange D, Saanouni K (2021) Thermomechanical model for solidification and cooling simulation of Ni-based superalloy components. Int J Solids Struct 212:202–219

12. Panwisawas C, Gebelin JC, Warnken N, Broomfield RW, Reed RC (2011) Numerical modelling of stress and strain evolution during solidification of a single crystal superalloy. Adv Mater Res 278:204–209. https://doi.org/10.4028/www.scientific.net/AMR.278.204

13. Galles D, Lu J, Beckermann C (2019) Determination of pattern allowances for steel castings using the finite element inverse deformation analysis. Int J Cast Met Res 32(3):123–134. https://doi.org/10.1080/13640461.2018.1558562

14. Qiu F, Bu K, Song J-H, Tian G-L, Zhang X-D (2018) Dimensional control of nickel-based single crystal turbine blade investment casting by process control optimization. Int J Met 12(3):469-479

15. Galles D, Beckermann C (2017) Effect of sand dilation on distortions and pattern allowances during steel sand casting. Int J Cast Met Res 30(5):257–275. https://doi.org/10.1080/13640461.2017.1290909

16. Yan J, Chen L, Liao D, Lin H, Liu R (2004) Study on numerical simulation of casting thermal stresses based on FDM. Acta Mater Sinica 17(1):7–10

17. Behera MM, Pattnaik S, Sutar MK (2019) Thermo-mechanical analysis of investment casting ceramic shell: a case study. Measurement 147:106805. https://doi.org/10.1016/j.measurement.2019.07.033

18. Neto R, Duarte T, Alves JL, Torres F (2017) Experimental characterization of ceramic shells for investment casting of reactive alloys. Ciencia & Tecnologia dos Materiais 29(1):34–39

19. Sundararaman M, Mukhopadhyay P, Banerjee S (1988) Precipitation of the δ-Ni3Nb phase in two nickel base superalloys. Metall Trans A 19(3):453–465

20. Lu Z, Chen Y, Miao K, Xu W, Liu T, Yang Q, Li D (2018) Microstructures and high-temperature strength of gel-casting Al2O3-based ceramic molds with coated aluminum additive. Int J Adv Manuf Technol 94(1):845–854. https://doi.org/10.1007/s00170-017-0930-9

21. Lu Y, Liu X, Lü K, Li Y, Liu F, Liu P (2021) Properties and fracture surface features of plaster mold reinforced with short polypropylene fibers for investment casting. Int J Met 15(2):700–709. https://doi.org/10.1007/s40962-020-00505-3

22. Kanka B, Schneider H (2000) Aluminosilicate fiber/mullite matrix composites with favorable high-temperature properties. J Eur Ceram Soc 20(5):619–623. https://doi.org/10.1016/S0955-2219(99)00260-5

23. Pattnaik S, Sutar MK (2022) Preparation and analysis of a hybrid ceramic shell for investment casting. Int J Adv Manuf Technol 122(5–6):2513–2527

24. Nawrocki J, Szeliga D, Kubiak K, Matysiak H, Motyka M, Ziaja W (2015) Influence of process parameters on cooling conditions in nickel base superalloy investment casting. Key Eng Mater 641:124–131. https://doi.org/10.4028/www.scientific.net/KEM.641.124

25. An LJ, Peirce A (1994) The effect of microstructure on elastic-plastic models. SIAM J Appl Math 54(3):708–730. https://doi.org/10.1137/s0036139992238498

26. Mandziej, ST (2005): In: Böllinghaus T, Herold H (eds) Testing for susceptibility to hot cracking on Gleeble^TM physical simulator, pp 347–376. Springer, Berlin, Heidelberg. https://doi.org/10.1007/3-540-27460-x_18